EBSD characterization of nano/ultrafine structured Al/Brass composite produced by severe plastic deformation

Majid Naseri,1, Mohsen Reihanian1, Ehsan Borhani2*

1Department of Materials Science and Engineering, Faculty of Engineering, Shahid Chamran University of Ahvaz, Ahvaz, Iran.

2Department of Nano Technology, Nano Materials Group, Semnan University, Semnan, Iran.

ABSTRACT

In the present work, nano/ultrafine structured Al/Brass composite was produced by accumulative roll bonding (ARB) up to eight cycles. The evolution of grain refinement and deformation texture and their effect on the mechanical properties were investigated. It was observed that by increasing the ARB cycles, due to the difference in flow properties of the metal constituents, brass layers necked, fractured and distributed in aluminum matrix. After eight cycles, a composite was produced with almost homogeneous distribution of brass fragments in aluminum matrix. Microstructural characterization by electron backscatter diffraction (EBSD) revealed the formation of bimodal structure consisting of equiaxied grains with an average size of ~120 nm and elongated grains after eight cycles, which was attributed to the occurrence of redundant shear and recrystallization. The crystallographic texture results indicated that the major texture components in the aluminum matrix were Brass {011}<211>, S {123}<634>, Goss {011}<100> and Rotated Goss {011}<011>. Moreover, it was concluded that Goss {011}<100> and Rotated Goss {011}<011> components appeared for high number of ARB cycles due to the adiabatic heat during ARB processing. The tensile strength of Al/Brass composite reached 330 MPa, which was 4.23 times and 1.83 times higher than those of annealed aluminum and monolithic aluminum, respectively. Finally, fracture surfaces of samples were studied, using field emission scanning electron microscope (FESEM), to reveal the failure mechanism.

Keywords: *Aluminum matrix composites (AMCs); Accumulative roll bonding (ARB); Electron backscatter diffraction (EBSD); Microstructure characterization; Deformation texture; Mechanical properties.*

1. Introduction

Strong materials are a classical goal for materials research and development. Nowadays there is a focus on nano/ultrafine grained (NG/UFG) metals because they are found to have a very high strength as well as other excellent mechanical properties [1, 2]. NG/UFG metals can be processed by a number of different techniques while one promising method is to apply intense plastic deformation in to the material. Though numerous methods for imposing large plastic strain like equal channel angular pressing (ECAP) [3], high pressure torsion (HPT) [4], multi directional forging (MDF) [5],

twist extrusion (TE) [6], repetitive upsetting and extrusion (RUE) [7] have been proposed, only few methods exclusively have been purported for processing fine grained materials in sheet forms. These methods include constrained groove pressing (CGP) [8], repetitive corrugation and straightening (RCS) [8], accumulative roll bonding (ARB) [9, 10] and cross accumulative roll bonding (CARB) [11].

ARB involves stacking two sheets of the same materials after proper annealing and surface treatments and rolling to the reduction of 50%. The rolled sheet is cut into two equal halves, and this cycle is repeated as many times as needed, so that

a large strain can be accumulated in the metallic sheet during the ARB without any sheet geometrical change [9, 10]. In comparison to conventional processes, the ARB has several advantages that include [9, 10]: (a) lower load capacity, (b) higher productivity rate, and (c) large amount of produced material. Over the last decades, the evolution of microstructures and the related mechanical properties during ARB were studied for several metals such as aluminum [9, 10, 12-16], copper [17], brass [18], titanium [19], nickel [20] and steel [21-24]. ARB is also a novel and applicable method in the production of multilayered metallic composites containing different components such as Al/Cu [25], Al/Ni [26], Al/Ti [27], Al/steel [28, 29] and Al/Ti/Mg [30]. Metal matrix composites (MMCs) with different conventional reinforcing ceramic particles including Al_2O_3 [31, 32], SiC [33], B_4C [34], ZrO_2 [35], TiC [36], and hybrid metal matrix composites (HMMCs) containing two reinforcing particles such as Al_2O_3/SiC [37], Al_2O_3/TiC [38], B_4C/SiC [39-42] and WO_3/SiC [43] are also successfully fabricated by ARB.

Multilayered metallic composites incorporating different metals belong to a new class of materials. These type of composites, combine the advantages of the constitutive metals to achieve better properties. In other words, a combination of mechanical, electrical, electrochemical and magnetic properties can be obtained for the composite material that cannot be obtained for the individual metals [26, 28, 30, 44]. During the co-deformation of dissimilar layered metal systems, plastic instabilities in one layer happen earlier than the others due to differences in mechanical properties [45, 46]. Recently, the critical strain for the onset of necking and fracture in the harder layer during ARB of metallic multilayer has been predicted by Reihanian and Naseri [47]. Although lots of works have been performed for fabrication and mechanical characterization of different multilayered metallic composites processed by ARB, little work on the texture development has been reported till date [48, 49]. It is known that during rolling, the metals deform inhomogeneously through thickness due to the large amount of shear strain that is introduced into the surface and subsurface regions. Furthermore, half of the surface region is folded to the center in the next ARB cycle and such a procedure is repeated as the cycles of ARB increase [50, 51]. According to the literature, the texture evolution in bimetallic

systems produced by ARB has received a limited attention and confined to such special cases as Fe/Ni [52], Cu/Ta [53], Zr/Nb [54, 55] and Cu/Nb [56].

Al/Brass composites have great potential for industrial applications in automobile and electronics industry due to their excellent mechanical properties and high specific conductivity combined with low density. Al/Brass is a potential alternative to pure copper for automotive applications in power cables, including battery cables and power leads to electronic components because it offers a lightweight alternative that provides superior conductivity. In addition, the Al/Brass system is economically more attractive than monolithic brass by the joining of relatively inexpensive aluminum. The advantage of using the aluminum and brass couple is that the aluminum matrix has a relatively low density and the brass fragments increase the strength of the composite. Therefore, a composite with a relatively high specific strength (strength to weight ratio) is produced. In the present work, the feasibility of the ARB method for the fabrication of the Al/Brass composites is examined for the first time. Although, the texture and deformation mechanisms in aluminum and brass alloys have been investigated individually [57-59], however, the simultaneous deformation of aluminum and brass in the form of a bimetallic system and the severe strain imposed by the ARB can affect the texture and microstructure. Hence, the microstructure, texture and mechanical properties of the composite are systematically investigated by electron backscatter diffraction (EBSD), uniaxial tensile tests and microhardness measurements. In particular, based on the orientation distribution functions (ODFs) obtained by EBSD analysis, the crystallographic texture of the composites is considered in details.

2. Material and methods
2.1. Research material
The materials utilized in this study were commercially pure aluminum and brass alloy (in the form of sheets) with thickness of 1.0 and 0.8 mm, respectively. The whole compositions of the materials are provided in Table 1. The sheets were cut into 150 mm × 50 mm strips, parallel to the sheet rolling direction. Annealing was then conducted at 370 °C for 2 h (for aluminum) and at 600 °C for 2 h (for brass) to remove the effects of deformation induced during the previous step of

materials processing.

2.2. Accumulative roll bonding process

In the first round, after surface preparation (the time interval was kept less than 120 s), the sheets were stacked in the manner of two aluminum layers as the outer surfaces and one brass layer as the inner surfaces. The stacked laminates were fastened by copper wires on the four edges. Sandwiches with thickness of about 1.0 mm were prepared by cold rolling through a 64% reduction in thickness by one cycle. Then, for the second round, sandwiches were cut into two halves, degreased, wire brushed, stacked and fixed. The strip was roll-bonded with a draft percentage of 50% reduction. The process was carried out at room temperature and repeated up to eight cycles. The roll bonding process was accomplished with no lubrication, using a laboratory rolling mill with diameter of 170 mm, loading capacity of 35 t and the rolling speed of 4 rpm.

2.3. Microstructural evaluations

Electron backscatter diffraction in a scanning electron microscopy equipped with a field emission type gun (SEM Philips XL30S-FEG) was used in order to characterize microstructure and crystallographic feature of the specimens. The section of the specimen was prepared by mechanically and then electrolytically polishing in a 30% HNO_3 and 70% CH_3OH solution at approximately 30 °C with a voltage of 15V for EBSD observation. The EBSD measurements were carried out with a step size of 50 nm and the obtained data was analyzed by TSL-OIM analysis software. For microstructural analysis, transfer direction (TD) of the samples was used. Crystallographic texture was evaluated by measuring incomplete pole figures of {111}. In order to obtain appropriate EBSD observation for texture evolution, the relatively large area of the specimen's section having more than 500 grains was considered. For a better understanding of the texture evolution, the face-centered cubic (FCC) fibers were calculated directly from the ODFs.

2.4. Mechanical properties

The tensile test specimens were machined along the rolling direction from the produced composites. The gauge width and length of the tensile samples were 5 ± 0.1 mm and 10 ± 0.1 mm, respectively. The tensile tests were carried out at an ambient temperature and at a nominal strain rate of 10^{-3} s^{-1} by a SANTAM STM-50 tensile testing machine. Moreover, the total elongation of each specimen was measured from the difference in the gage length before and after testing. To verify the accuracy of results, three tensile tests were performed for each specimen. Also, to investigate the fracture behavior of the surfaces after the tensile test, VEGA\\TESCAN field emission scanning electron microscope (FESEM) equipped with an energy dispersive spectroscope (EDS) characterization was performed.

Vickers microhardness of the samples was measured by using a Nexus Innova 4300 microhardness testing machine under a load of 15 g and time of 15 s on the cross section surface of composites perpendicular to rolling direction. Microhardness was measured randomly at nine different points on aluminum matrix and brass layers. The maximum and minimum values were disregarded and the mean hardness value was calculated from the remaining seven values.

3. Results and discussion
3.1. Microstructure characterization

Fig. 1 illustrates microstructure variations of Al/Brass composites on rolling direction-normal direction (RD-ND) plane after different ARB cycles.

Table 1- Chemical composition (wt.%) of the aluminum and brass strips used in this study

Al 1050									
Al	Si	Fe	Cu	Mn	Mg	Zn	Cr	Ni	Ti
97.3	0.588	0.762	0.189	0.732	0.189	0.129	0.0123	0.0058	0.0329
Be	Ca	Li	Pb	Sn	Sr	V	Na	Bi	Zr
< 0.0001	< 0.0009	< 0.0001	0.0049	0.0021	< 0.0001	0.0117	0.0043	< 0.005	< 0.002
B	Ga	Cd	Co	Ag	Hg	In			
0.005	0.0041	< 0.001	< 0.003	< 0.001	< 0.003	< 0.01			
Brass									
Cu	Zn	Pb	Sn	P	Mn	Fe	Ni	Si	Mg
61.3	38.4	< 0.005	< 0.005	< 0.003	0.0043	0.0269	0.0055	0.0183	0.0052
Cr	Al	S	As	Ag	Co	Bi	Cd	Sb	Zr
0.0024	0.0042	0.0074	0.0024	0.006	0.0088	0.0191	0.0009	0.0081	0.0036

It is evident that brass layers are coherent just in the first cycle of composite production, and then they initiate to neck and fracture locally in subsequent cycles. As ARB proceeded, strain is increased and thickness of brass layers is decreased. Consequently, brass layer separation is observed in the fourth cycle. Finally, after eight cycles, an aluminum matrix composite with almost homogeneously distributed brass fragments in the matrix is achieved. The type of composite shown in Fig. 1 has been also considered in the previous works. Talebian and Alizadeh [28] investigated the effects of subsequent annealing on the microstructural and mechanical characteristics of Al/steel multilayered composite produced by ARB process. Also, Mohammad Nejad Fard et al. [29] produced an Al/Stainless Steel/Al

composite sheets by roll bonding of the starting sheets at 400 °C. Afterward, the roll bonded sheet was cut in half and the accumulative roll bonding (ARB) process at room temperature was applied. They showed that the central steel layer fractured and distributed in the aluminum matrix among different layers introduced by the repetition of roll bonding process.

In general, necking and fracture take place in the hard phase due to simultaneous deformation of dissimilar metals and the difference in flow properties of the metal constituents [26, 27, 30]. The plastic instability is controlled by the initial thickness ratio, strength coefficients and work hardening exponents of the layers [45, 47]. To compare the flow properties of the constituents, the
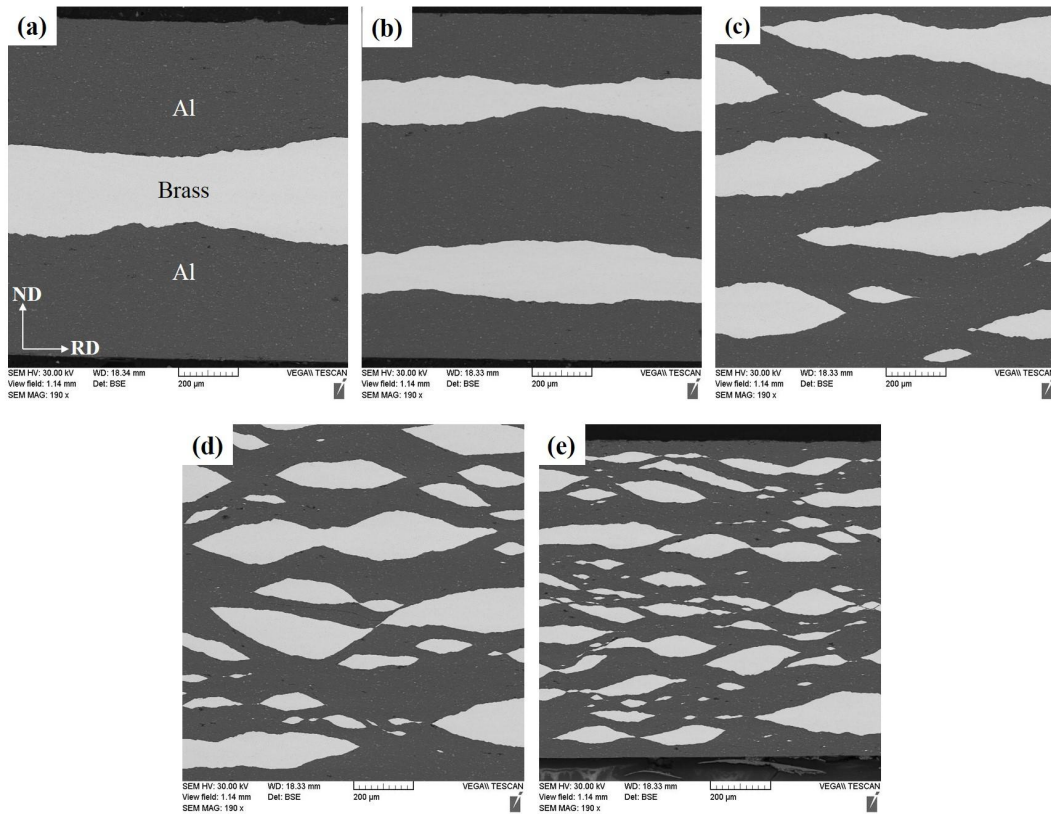

Fig. 1- SEM micrographs of ARB processed Al/Brass composite after (a) one, (b) two, (c) four, (d) six and (e) eight cycles.

Table 2- Flow properties of the annealed aluminum and brass

Element	Work hardening exponent	Coefficient of strength (MPa)	Tensile strength (MPa)
Aluminum	0.284	145	78
Brass	0.572	645	365

strength coefficient, k, work hardening exponent, n, and tensile strength for aluminum and brass are summarized in Table 2. These values are obtained from tensile test after annealing of each specimen.

It is seen that brass has the higher work hardening exponent (0.337) and larger tensile strength (365 MPa) compared with that of aluminum. As a result, necking of brass as the harder phase is reasonable.
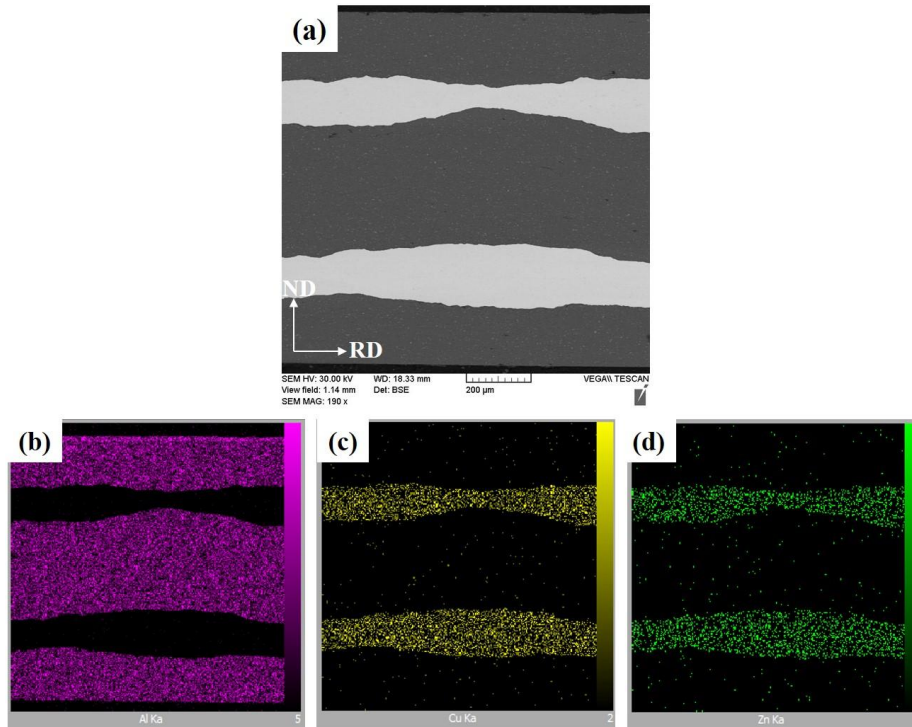

Fig. 2- SEM image of Al/Brass composite after two ARB cycles and the corresponding SEM elemental maps for (b) Al distribution, (c) Cu distribution and (d) Zn distribution.
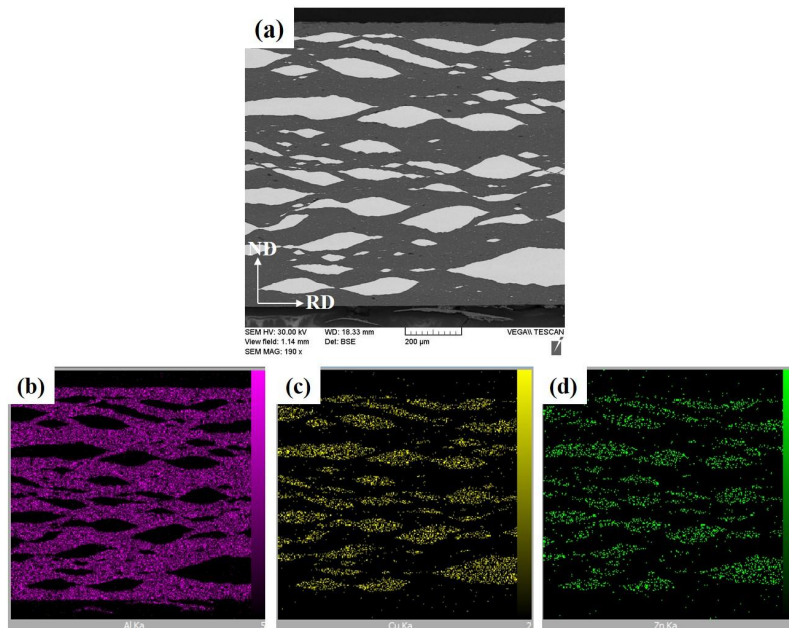
Fig. 3- SEM image of Al/Brass composite after eight ARB cycles and the corresponding SEM elemental maps for (b) Al distribution, (c) Cu distribution and (d) Zn distribution.

Necking in the hard phase has also been reported in other multilayer systems processed by ARB is proceeds [25, 26, 30, 46, 47, 53].

In order to investigate the distribution of brass layer, SEM/elemental maps of the Al/Brass composite after two and eight ARB cycles are obtained and the results are presented in Figs. 2 and 3. After the second cycle (Fig. 2), the extension of necking in brass layers is concurrent along about 45° to the rolling direction. As the ARB processes (Fig. 3), necking, rupturing and fragmentation of brass layers are confirmed by the SEM/elemental maps and the brass fragments are distributed more uniformly in the aluminum matrix.

The image quality (IQ), orientation color and the corresponding grain boundary maps of the annealed aluminum and Al/Brass composite processed to eight cycles are displayed in Fig. 4. Image quality maps obtained from EBSD data provide useful visualizations of microstructure. The contrast in these maps arises from a variety of sources, including phase, strain, topography and
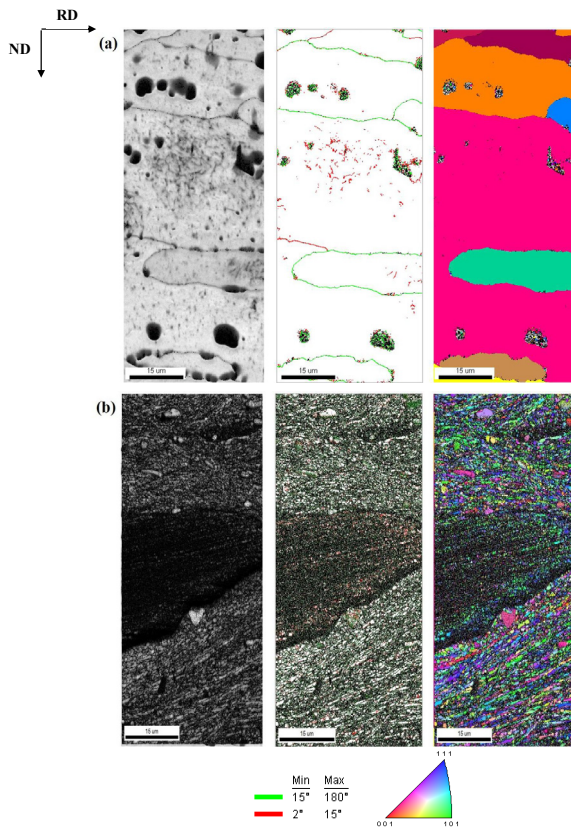
grain boundaries [60]. In color maps, the colors within the grains correspond to the orientations of each grain as depicted by the unit triangle at the bottom of the figure. In boundary maps, high angle grain boundaries (HAGBs) with misorientation angles higher than 15° are depicted by green lines, while low angle grain boundaries (LAGBs) with misorientation angles of 2–15° are denoted by red lines. The initial grain size before deformation is about 30 μm, using the linear intercept method in the normal direction of the elongated grains (Fig. 4(a)). With attention to Fig. 4(b), the structure contains of mostly ultrafine grains surrounded by semi-lamellar boundaries form a bamboo-like structure [13, 61, 62]. The grain boundaries have mostly high angle grain boundaries having misorientation angle lager than 15°.

The fraction of high angle grain boundaries (f_{HAGB}) and the mean misorientation angle of the boundaries (θ_m) were calculated from the EBSD data of each specimen (Fig. 5). The f_{HAGB} and the θ_m for the annealed aluminum are 54% and 21.40°, respectively, while for those of the Al/Brass composite after eight cycles are 79% and 34.87°, respectively. The EBSD analysis shows that the large grains of the annealed aluminum subdivided to

Fig. 4- The image quality, grain boundary and orientation color maps of the (a) annealed aluminum and (b) Al/Brass composite after eight cycles.
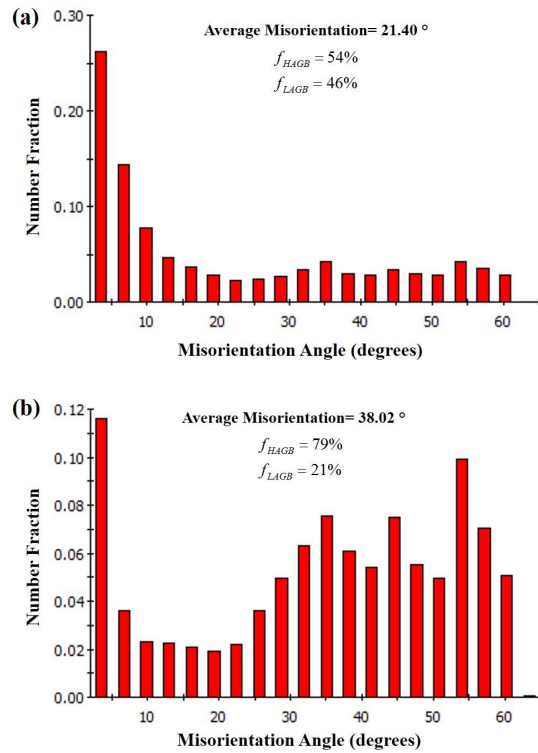

Fig. 5- The misorientation angle distribution of the (a) annealed aluminum and (b) Al/Brass composite after eight cycles.

nano/ultrafine grains and the low angle boundaries are transformed to high angle ones. This is the main reason as to why the density of low angle grain boundaries has been decreased and the structure in this case contains substantial amount of high angle grain boundaries [13, 15, 19, 50, 51, 62].

Image quality map at high magnification, grain boundary analysis, grain size distribution profile, rolling direction and normal direction orientation color maps of aluminum in Al/Brass composite obtained by EBSD measurements after eight cycles are shown in Fig. 6. Clear waviness is shown in this figure, which is due to the formation of shear bands during the ARB [46, 50]. These localized shear bands are inclined at 30 to 40° to the RD throughout the sample thickness. According to the literature [63], the shear bands are narrow regions in which intense shear occurs as a result of plastic instability. In this investigation, the formation of the shear bands is as a result of the large difference in flow properties between the brass and the aluminum layers. Also, it is seen that a bimodal structure consisting of equiaxied and elongated aluminum grains is formed after eight cycles. The average grain size of equiaxied grains reached 120 nm indicating considerable grain
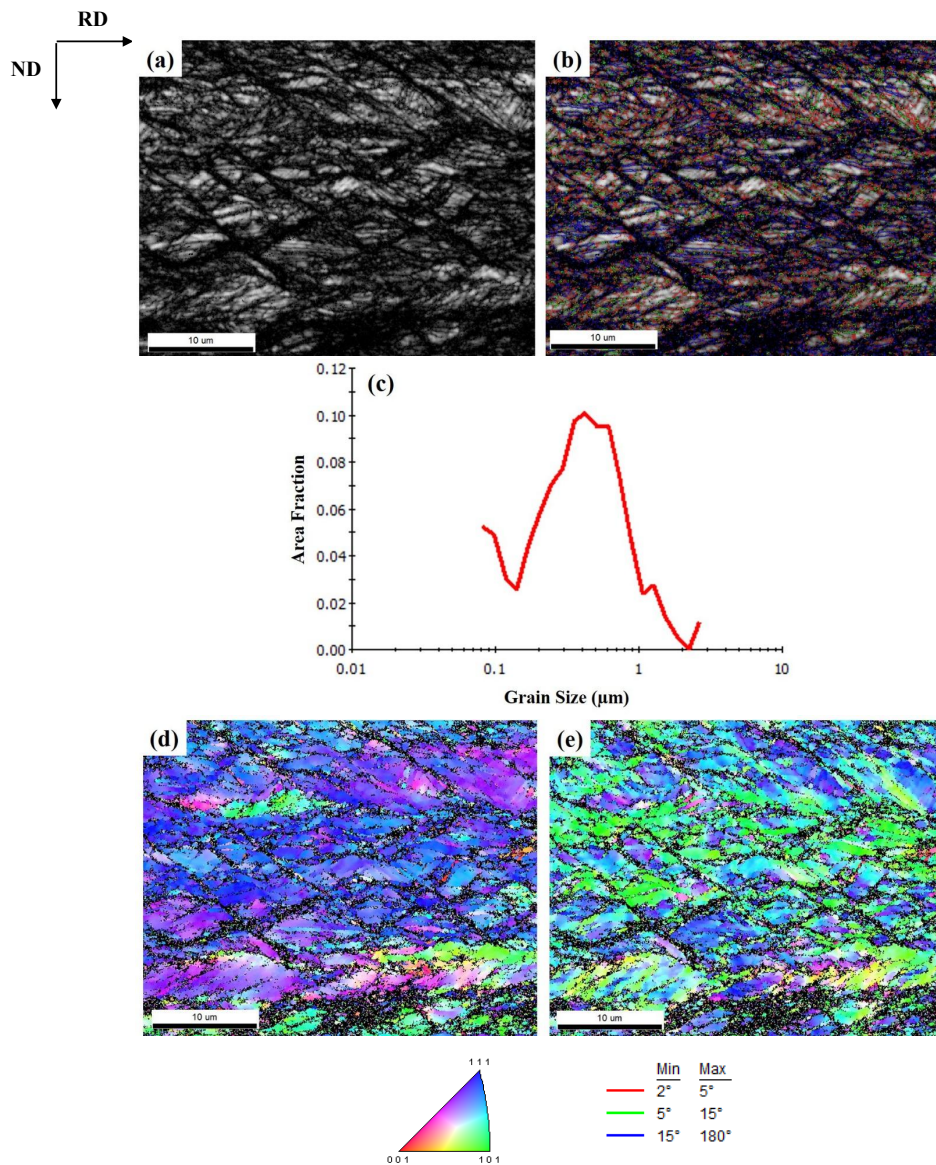
Fig. 6- Microstructure of the aluminum side in Al/Brass composite after eight cycles at high magnification: (a) image quality map, (b) grain boundary map, (c) grain size distribution profile, (d) RD orientation color map and (e) ND orientation color map.

refinement occurred after eight ARB cycles. Also, the nanometric grains (smaller than 100 nm) can also be observed. Formation of nano/ultrafine grains has also been reported in the ARB processed materials, particularly for single phase alloys [22, 23, 50, 62]. The color maps of the specimen indicate that preferred orientation develops by eight cycles, as particular colors become dominant in the orientation color maps. The ND orientation color map of the composite demonstrates green color as dominant color corresponding to <110>//ND. This means that the surface area has <110>//ND α-fibre texture.
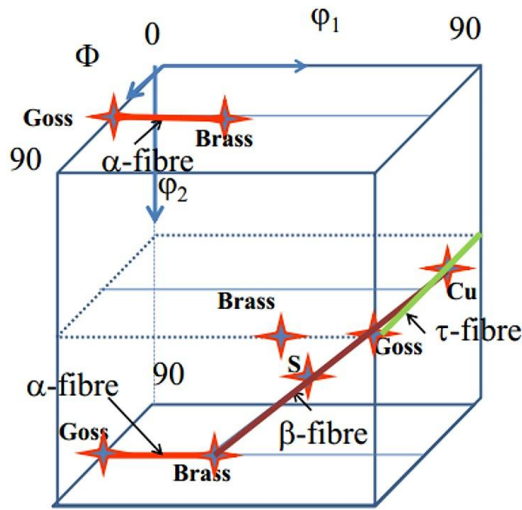
Fig. 7- Schematic illustration of important fibers in the FCC materials.

3.2. Deformation texture

Texture in deformed sheets with cubic crystal structures are usually presented by the expression of {hkl}<uvw>, where {hkl} is the Miller indices of the crystallographic plane parallel to the rolling plane and <uvw> is the Miller indices of the crystallographic direction parallel to the rolling direction. The ideal orientations of texture components and important fibers in FCC materials are shown in Table 3 and Fig. 7. The most relevant texture fibers for FCC materials are as follows [64-66]:

1- α-fiber (crystallographic fiber axis <110>parallel to the normal direction, 0°,45°,0°—90°,45°,0°): Extends from Goss {011}<001> to Brass {011}<112> orientation.

2- β-fiber (defined by the maximum intensity rather than by exact crystallographic position, 90°,35°,45°—35°,45°,90): Extends from Copper {112}<111> to S {123}<634> to Brass {011}<112> orientation.

3- τ-fiber (fiber axis <110> parallel to the transverse direction, 90°,0°,45°—90°,90°,45°): Extends from Rotated Cube {001}<110> to Copper {112}<111> to Goss {011}<001> orientation.

The detailed analysis of texture evolution of the annealed aluminum and the Al/Brass composite samples processed by various ARB cycles is shown as ODFs in Fig. 8. The φ_2 = 0°, 45° and 65° sections are presented since they contain all relevant FCC deformation texture components. As shown in Fig. 8(a), the texture components of the annealed aluminum can be characterized as

Table 3- Euler angles and Miller indices for important texture components in FCC materials

Texture component	Miller indices	Euler angles			Fiber
		φ_1	ϕ	φ_2	
Cube	{001}<100>	0	0	0	Cube-Goss/θ
Rotated Cube	{001}<110>	45	0	0	θ
Goss	{011}<100>	0	45	0	Cube-Goss/α/τ
Rotated Goss	{011}<011>	90	45	0	α
Goss Twin	{113}<332>	90	25	45	τ
Brass	{011}<211>	35	45	0	α/β
Goss/Brass	{011}<115>	16	45	0	α
A	{011}<111>	55	45	0	α
Y	{111}<112>	90	55	45	γ/τ
E	{111}<011>	60	55	45	γ
Copper	{112}<111>	90	35	45	τ/β
Rotated Copper	{112}<011>	0	35	45	-
Copper Twin	{554}<115>	90	74	45	τ
Dillamore	{4 4 11}<11 11 8>	90	27	45	τ
S	{123}<634>	59	37	63	β
S/Brass	{414}<234>	49	40	75	β

the Cube {001}<100>, Brass {011}<211> and S {123}<634> components with maximum intensity of 4.4 × R, 6.4 × R and 4.3 × R, respectively. After one cycles (Fig. 8(b)), Brass {011}<211> and S {123}<634> components disappeared and the Goss {011}<100> is created. The dominant components are Goss {011}<100> and Cube {001}<100> with the maximum intensity of 6.1 × R and 2.3 × R, respectively. After the fourth cycle (Fig. 8(c)), the Goss {011}<100> and Cube {001}<100> components disappeared and the Rotated Goss {011}<011>, Brass {011}<211> and S {123}<634> components appeared. Finally, after eight cycles (Fig. 8(d)), the Goss {011}<100> component with maximum intensity of 16.4 × R is created again and the intensity of the Rotated Goss {011}<011>, Brass {011}<211> and S {123}<634> increased to 15.3 × R, 18.5 × R and 12.4 × R, respectively.

According to ODFs shown in Fig. 8, after eight ARB cycles, a mixed deformation/recrystallization texture is observed. It is well accepted that in the absence of recrystallization, plane strain deformation of aluminum metals, such as that encountered in the rolling process, the texture develops around the Copper {112}<111>, Brass {011}<211> and S {123}<634> orientations [65- 66]. In metals with a low or medium stacking fault energy (SFE) (copper, brass and austenitic iron) in which recovery processes are slow, recrystallization may take place when a critical deformation condition is reached [52, 57, 58, 65]. Even though the current ARB is performed at ambient temperature, the temperature inside the Al/Brass samples generally increased through the adiabatic heat during heavy deformation. Meanwhile, as the amount of strain increases, recrystallization occurs at a lower temperature and in a shorter time [65]. Thus, more recrystallization will take place in the higher ARB cycles. The recrystallization of the Al/Brass composite also contributes to the formation of equiaxed grains (Fig. 6) instead of forming the laminar grains at the higher ARB cycles. Therefore, it is reasonable that appearing the Goss {011}<100> and Rotated Goss {011}<011> orientations in
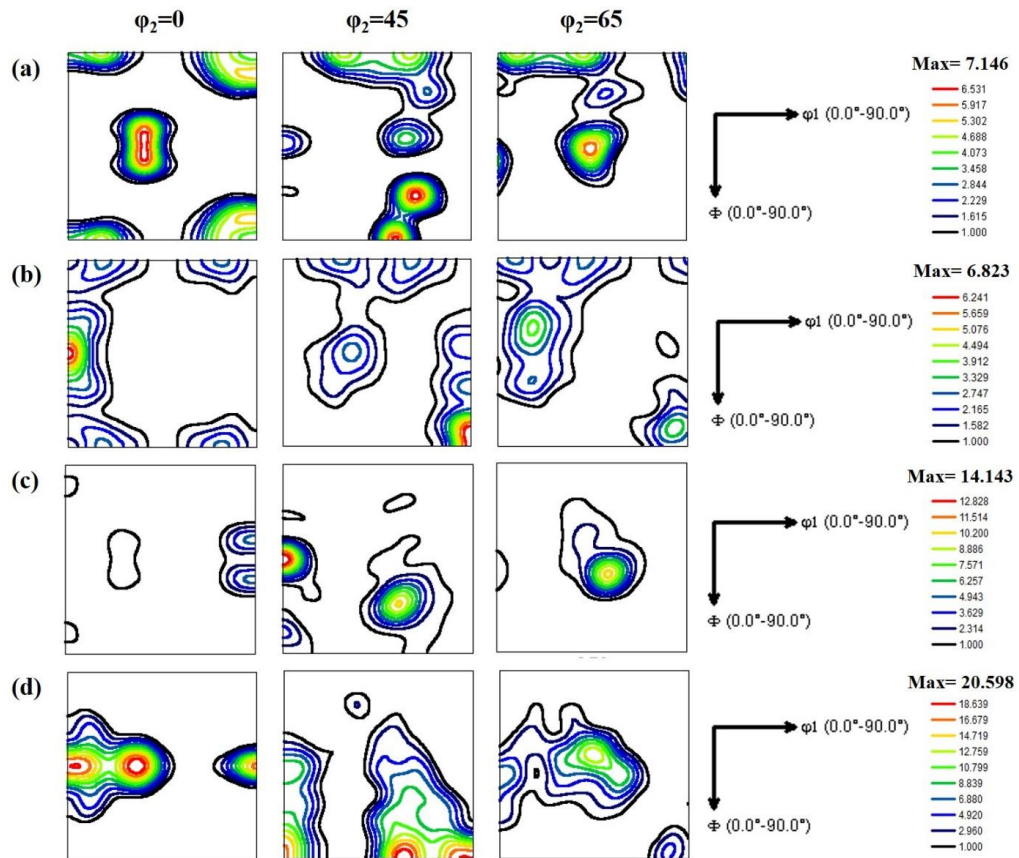

Fig. 8- The ODF sections of constant (0º, 45º and 65º) showing the texture components in the (a) annealed aluminum and Al/Brass composite after (b) first, (c) fourth and (d) eighth ARB cycles.

Al/Brass composite is attributed to the occurrence of recrystallization [65].

Texture evolution can be clarified more by showing the fibers during the process by skeleton lines. Therefore, the orientation density (f(g)) of main FCC fibers including α, β and τ was calculated from ODFs, as plotted in Fig. 9. It can be seen that the intensity of α-fiber for the first ARB cycle is very weak, after the fourth cycles is strong, and after the eighth cycles is very strong (Fig. 9(a)). In other words, the intensity of α-fiber increases with increasing the number of ARB cycle. Also, there is a texture transitions in the α-fiber from Goss {011}<100> to Brass {011}<211> after the fourth cycle. Fig. 9(b) indicates that there is a texture transition in the β-fiber after the fourth cycle. It is obvious that the dominant orientation at the first cycle is Copper {112}<111> texture component; but after the fourth ARB cycle the dominant orientation changes to S {123}<634> component. Also, when the number of ARB cycles increases, first, the intensity of β-fiber greatly increases and then slightly decreases. The textural

evolution of τ-fiber is centered mainly around the Dillamore {4 4 11}<11 11 8> and Goss {011}<100> components (Fig. 9(c)). When the number of ARB cycles increases, the intensity of τ-fiber decreases and then slightly increases. The fact that the intensities of the cold rolling β-fiber texture and τ-fiber texture do not increase with increasing the number of ARB cycles can be attributed to the effect of the shear bands [50, 52, 58]. The shear bands are confirmed in the EBSD images (Fig. 6). Quadir et al. [67] discovered the 15° deviation of aluminum texture from rolling direction due to the shear stress between rolled pure aluminum and Al–Sc alloy layers. This crystallographic rotation led to a spread of orientations around the TD, and decreased both intensity and sharpness of the aluminum rolling fiber textures. This phenomenon was also observed by Chang et al. [68] during the ARB of Mg/Al composites.

Generally, in this research, due to the presence of large fragments of brass in the aluminum matrix, the intensity is weak for all the texture components. Borhani et al. [64] indicated in their studies that
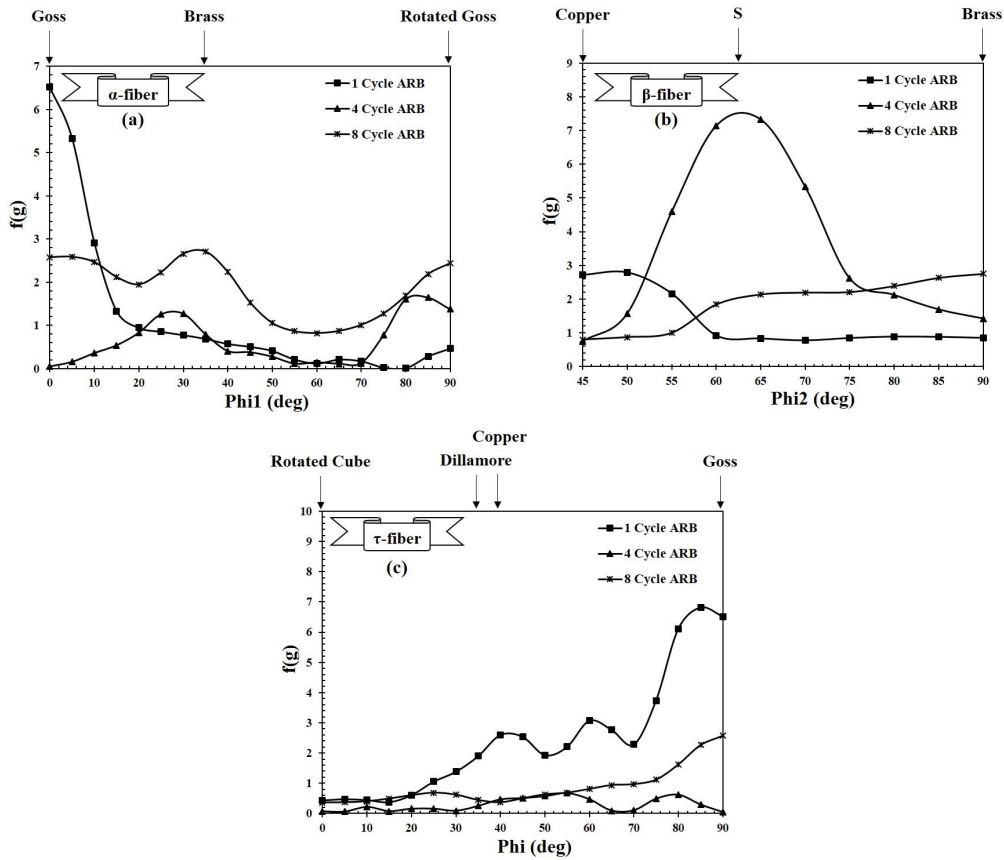

Fig. 9- Fibers developed during ARB for Al/Brass composite: (a) α-fiber, (b) β-fiber and (c) τ-fiber.

an inhomogeneous deformation generates the deformation zone near large second phase particles and precipitates. Therefore, the weak texture of the ARB processed composites can be related to the formation of mentioned deformation zone in the matrix. Particularly, extensive pileups of dislocations can be caused by non-shearable large particles, resulting in the formation of deformation zones around the particles [65], which lead to reduced texture intensity. Hence, in accordance with previous studies [48], it is concluded that the observed weak texture is due to an inhomogeneous deformation around the large particles.

3.3. Mechanical properties

The engineering stress–strain curves of the annealed aluminum, monolithic aluminum and Al/Brass composite (after the eighth cycles) are shown in Fig. 10. Also, the variations of the tensile strength and the elongation with the number of rolling cycles for monolithic aluminum and Al/Brass composite are compared and plotted in Fig. 11. As can be seen in Fig. 11(a), the tensile strength is improved when the number of ARB cycles is increased for both monolithic aluminum and Al/Brass composite samples. The tensile strength of monolithic aluminum and Al/Brass composite is improved from 78 MPa (for the annealed aluminum) to 140 and 197 MPa for one cycle ARB processed samples, registering 80% and 153% increase, respectively. The first cycle has a remarkable effect on the tensile strength and is in a good agreement with previous researches [10, 14, 17, 18, 62, 69]. The tensile strength is increased continually until it becomes 2.30 times (180 MPa) and 4.23 times (330 MPa) higher than that of the
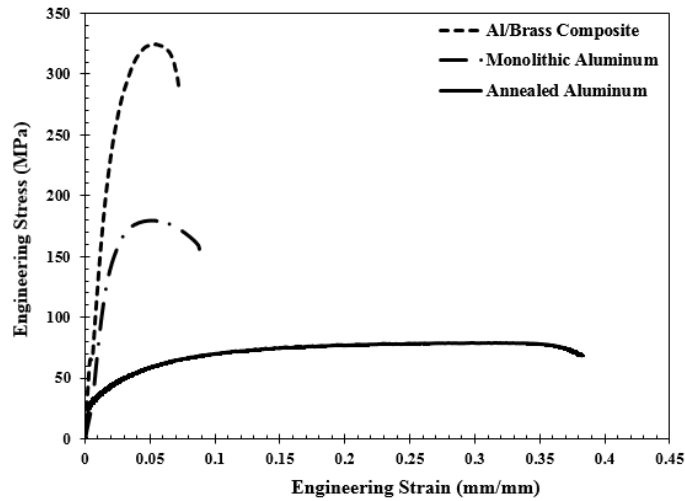

Fig. 10- Engineering stress–strain curves of the annealed aluminum, monolithic aluminum and Al/Brass composite specimens processed to eight cycles.
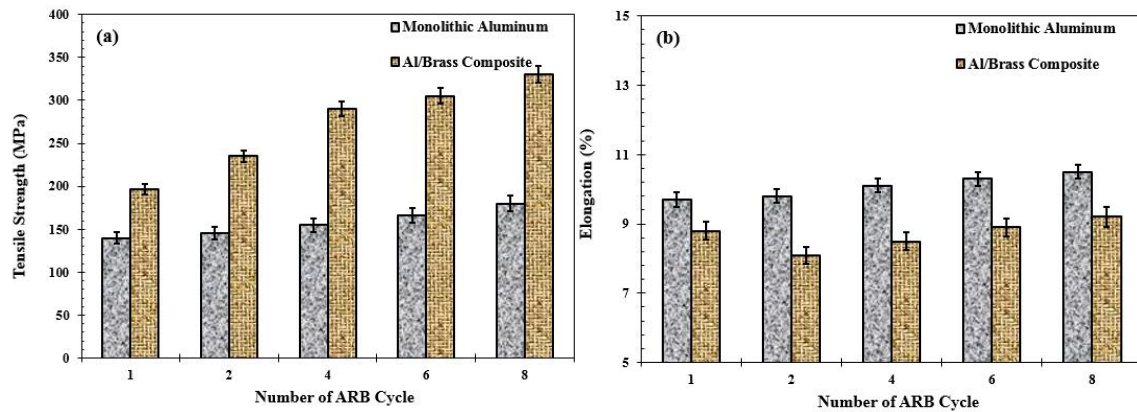

Fig. 11- Variations in (a) tensile strength and (b) elongation with the number of rolling cycles for monolithic and composite specimens.

annealed aluminum for monolithic aluminum and Al/Brass composite, respectively.

Strain hardening and grain boundary strengthening are two main mechanisms of strengthening during plastic deformation. At low to medium plastic strain, strain hardening occurs due the increase in dislocation density, dislocation interactions and accumulation and formation of dislocation boundaries. At large plastic strains, the flow stress is controlled by high angle grain boundaries and the grain boundary strengthening is the dominant mechanism [23, 28, 50, 70]. In the case of Al/Brass composite, the brass fragments act as reinforcing phase and provide the additional barriers to the motion of dislocations. Generally, the amount, shape, size and distribution of reinforcements affect the strength of the composite. During ARB, the fragmentation of brass layers occurs and the brass fragments gradually distribute in the aluminum matrix, causing the strength of the composite to increase with increasing the number of ARB cycle. The strain incompatibility between the matrix and reinforcement [63], the activation of the further slip systems at the interfaces [28, 53], and the difference in the thermal expansion coefficient of the phases [26, 30], can also lead to generation of dislocations and to increase the strength during ARB of the composite.

According to Fig. 11(b), the elongation of monolithic aluminum and Al/Brass composite significantly decreased from 36% (for annealed aluminum) to 9.7% and 8.8% after the first cycles, registering 73% and 76% decrease, respectively. The sharp decrease in the percent elongation of the monolithic aluminum and Al/Brass composite can be attributed to the strain hardening and accumulation of dislocations that lead to initiation of internal stresses and to the nucleation of cracks and cavities [33, 71]. At higher number of ARB cycle, the percent elongation of the monolithic aluminum remains approximately constant that can be due to the saturation in dislocation structure and dislocation density. However, the percent elongation of the Al/Brass composite increases to some extent at higher number of ARB cycle. It decreases to an amount of 8.1% after the second cycle while reaches to 9.2% after the eighth cycle. Several factors including the strain hardening, bonding at interface and distribution of the brass fragments can affect the elongation of the Al/Brass composite. Strain hardening leads to the accumulation of dislocations and internal stresses that promotes the nucleation of cracks and cavities, leading to the decrease in elongation. The sharp decrease of the elongation after two cycles can be attributed to the strain hardening of the Al/Brass composite. This trend can be observed by percent elongation at the initial stages of each severe plastic deformation process [30, 31]. In contrast, the increased bonding at the interfaces can increase the elongation through delaying the crack formation at the interfaces. In addition, the fragmentation and distribution of the brass layer leads to the increase in the net distance between the interfaces, reducing the probability of joining cracks. The latter two factors cause the uniform elongation of the Al/Brass composite to increase gradually as the ARB process is continued.

Microhardness variations of aluminum and brass layers at different cycles of ARB are shown in Fig. 12. The hardness of brass and aluminum in the annealed condition is about 87 HV and 27 HV,
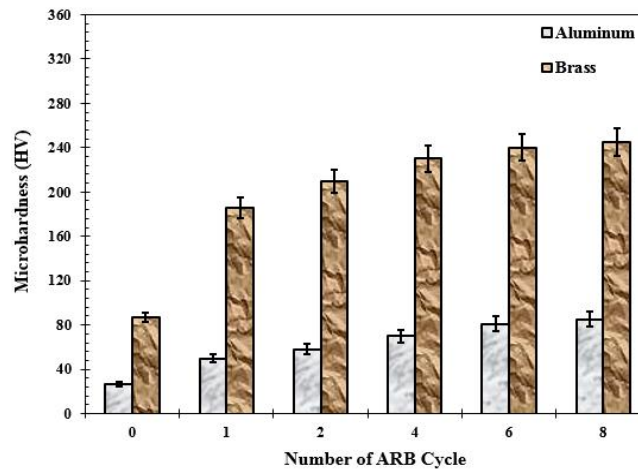

Fig. 12- Variation of microhardness for individual layers with different ARB cycles (0 cycle represents annealed specimens).

respectively. It is obvious that by increasing the ARB cycles, microhardness of brass is increased rapidly after the first ARB cycle and then it is saturated after the fourth cycle. For aluminum layers, microhardness (showing lower values than that of the brass layer) increases gradually through ARB up to the eighth cycle. These differences in microhardness values can be attributed to the difference in the strain hardening rate of aluminum and brass layers during plastic deformation. These observations may originate from different SFE of aluminum and brass (which are 166 mjm^{-2} and 20 mjm^{-2}, respectively [65]). In fact, metals with low to medium SFE (such as brass) hinder the climb and cross slip of dislocations (as two important phenomena for recovery process) as compared with the materials with higher SFE (such as aluminum). Thus, recovery is retarded for brass layers with lower SFE, thereby resulting in dislocation accumulation and greater work hardening. Similar observations for microhardness variations of metallic layers are also reported for Al/Cu [25], Al/Ni [26] and Al/ steel [28, 29] composites produced by the ARB.

3.4. Fractography

In order to clarify the rupture mechanisms of composites in different cycles of ARB, SEM was used. Fig. 13 illustrates the tensile fracture surfaces of the Al/Brass composite subjected to one, four and eight cycles. After one ARB cycles (Fig. 13a - b),
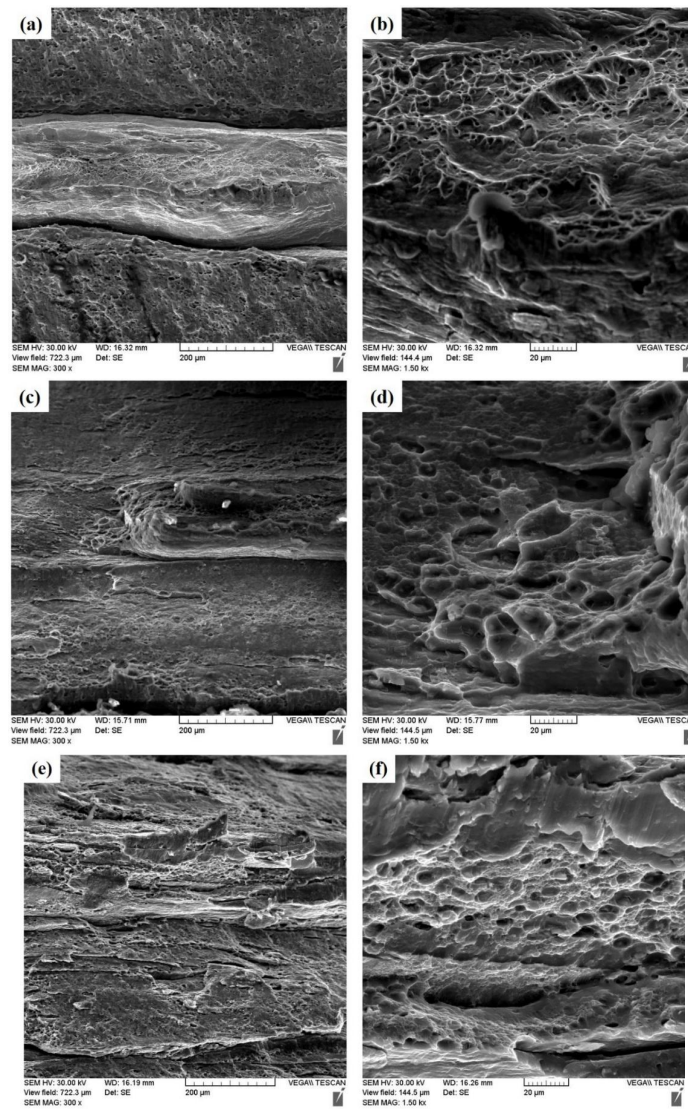

Fig. 13- Tensile fracture surfaces of Al/Brass composite after (a and b) first, (c and d) fourth and (e and f) eighth ARB cycles.

it is seen that the aluminum and brass layers are clearly distinguished. At this stage, the fracture appearance of the composite reveals dimples in aluminum and brass layers, indicating that the fracture mode is ductile in both layers. Dimple type fracture has also been observed in Al/Ti [72], Cu/Ni [73] and Al/Ti/Mg [30] systems. The ductile fracture takes place through the nucleation and coalescence of the microvoids ahead of the main crack [74]. After higher ARB cycles (Fig. 13(c and d)), it is somewhat difficult to identify the individual layers due to an increase in the layer number and a decrease in the layer thickness. However, some dimples are elongated in one or more directions. Also, few brittle fractures at the eighth cycle can be distinguished by considering Fig. 13(e and f). The shape and orientation of the dimples are influenced by the type of loading and the direction of the crack extension. The non-equiaxed dimples can be made by the non-uniform plastic strain, shear overloads and unequal triaxial stresses that become more probable at higher ARB cycles [14]. Fig. 13 also illustrates that by increasing ARB cycles, the bonding quality between layers is improved.

4. Conclusions

In the present study, accumulative roll bonding (ARB) is performed up to eight cycles at ambient temperature to manufacture the nano/ultrafine structured Al/Brass composite. The microstructure, deformation texture development and mechanical properties of the composite were investigated. The conclusions drawn from the results can be summarized as follows:

1. During ARB, the brass layer necks, ruptures and distributes uniformly in the aluminum matrix due to the dissimilar flow properties of the metal constituents. After eight ARB cycles, a composite of aluminum matrix with nearly uniform distribution of brass phase is obtained.

2. After eight ARB cycles, the major texture components in the Al/Brass composite are Brass {011}<211>, S {123}<634>, Goss {011}<100> and Rotated Goss {011}<011>. The development of the α-fiber and β-fiber texture is related to the dislocation structures introduced during successive ARB cycles.

3. The adiabatic heat during heavy deformation promotes the formation of the recrystallization texture components: Goss {011}<100> and Rotated Goss {011}<011>. The recrystallization retarded grain refinement and led to the formation of bimodal structure consisting of equiaxied grains and elongated grains for high ARB cycles.

4. The Al/Brass composite exhibits a relatively high tensile strength compared with the annealed aluminum so that the tensile strength of the composite is 4.23 times higher than that of the annealed aluminum. The increased strength of the composite is attributed to the strain hardening, grain refinement, uniformity of brass fragments in the aluminum matrix and good bonding at interfaces.

5. Microhardness of brass layers is greater for all cycles compared with that of aluminum layers. Also, with increasing the ARB cycles, the hardness of brass increases up to the fourth cycle and saturates at further number of ARB cycles. The aluminum layers exhibit a gradual increase from first to the last ARB cycle. The different trend in hardness variation is explained by the staking fault energy of the metal constituents.

6. Fracture analysis of tensile specimens shows that with increasing the number of ARB cycles, fracture mechanism is changed from ductile to shear ductile and partially, to brittle fracture at final cycles.

References

1. Meyers MA, Mishra A, Benson DJ. Mechanical properties of nanocrystalline materials. Progress in Materials Science. 2006;51(4):427-556.
2. Pande CS, Cooper KP. Nanomechanics of Hall–Petch relationship in nanocrystalline materials. Progress in Materials Science. 2009;54(6):689-706.
3. Iwahashi Y, Horita Z, Nemoto M, Langdon TG. The process of grain refinement in equal-channel angular pressing. Acta Materialia. 1998;46(9):3317-31.
4. Zhilyaev A, Langdon T. Using high-pressure torsion for metal processing: Fundamentals and applications. Progress in Materials Science. 2008;53(6):893-979.
5. Salishchev G, Zaripova R, Galeev R, Valiakhmetov O. Nanocrystalline structure formation during severe plastic deformation in metals and their deformation behaviour.

Nanostructured Materials. 1995;6(5-8):913-6.

6. Beygelzimer Y, Varyukhin V, Synkov S, Orlov D. Useful properties of twist extrusion. Materials Science and Engineering: A. 2009;503(1-2):14-7.

7. Zaharia L, Comaneci R, Chelariu R, Luca D. A new severe plastic deformation method by repetitive extrusion and upsetting. Materials Science and Engineering: A. 2014;595:135-42.

8. Huang JY, Zhu YT, Jiang H, Lowe TC. Microstructures and dislocation configurations in nanostructured Cu processed by repetitive corrugation and straightening. Acta Materialia. 2001;49(9):1497-505.

9. Saito Y, Utsunomiya H, Tsuji N, Sakai T. Novel ultra-high straining process for bulk materials—development of the accumulative roll-bonding (ARB) process. Acta Materialia. 1999;47(2):579-83.

10. Saito Y, Tsuji N, Utsunomiya H, Sakai T, Hong RG. Ultra-fine grained bulk aluminum produced by accumulative roll-bonding (ARB) process. Scripta Materialia. 1998;39(9):1221-7.

11. Kaneko S, Fukuda K, Utsunomiya H, Sakai T, Saito Y, Furushiro N. Ultra Grain Refinement of Aluminium 1100 by ARB with Cross Rolling. Materials Science Forum. 2003;426-432:2649-54.

12. Terada D, Houda H, Tsuji N. Effect of grain size distribution on mechanical properties of ultrafine grained Al severely deformed by ARB process and subsequently annealed. Journal of Physics: Conference Series. 2010;240:012111.

13. Naseri M, Reihanian M, Borhani E. A new strategy to simultaneous increase in the strength and ductility of AA2024 alloy via accumulative roll bonding (ARB). Materials Science and Engineering: A. 2016;656:12-20.

14. Naseri M, Reihanian M, Borhani E. Effect of strain path on microstructure, deformation texture and mechanical properties of nano/ultrafine grained AA1050 processed by accumulative roll bonding (ARB). Materials Science and Engineering: A. 2016;673:288-98.

15. Alvand M, Naseri M, Borhani E, Abdollah-Pour H. Nano/ultrafine grained AA2024 alloy processed by accumulative roll bonding: A study of microstructure, deformation texture and mechanical properties. Journal of Alloys and Compounds. 2017;712:517-25.

16. Borhani E, Jafarian H, Terada D, Adachi H, Tsuji N. Microstructural Evolution during ARB Process of Al-0.2 mass% Sc Alloy Containing Al3Sc Precipitates in Starting Structures. Materials transactions. 2012;53(1):72-80.

17. Shaarbaf M, Toroghinejad MR. Nano-grained copper strip produced by accumulative roll bonding process. Materials Science and Engineering: A. 2008;473(1-2):28-33.

18. Pasebani S, Toroghinejad MR. Nano-grained 70/30 brass strip produced by accumulative roll-bonding (ARB) process. Materials Science and Engineering: A. 2010;527(3):491-7.

19. Terada D, Inoue S, Tsuji N. Microstructure and mechanical properties of commercial purity titanium severely deformed by ARB process. Journal of Materials Science. 2007;42(5):1673-81.

20. Zhang YB, Mishin OV, Kamikawa N, Godfrey A, Liu W, Liu Q. Microstructure and mechanical properties of nickel processed by accumulative roll bonding. Materials Science and Engineering: A. 2013;576:160-6.

21. Kamikawa N, Tsuji N, Minamino Y. Microstructure and texture through thickness of ultralow carbon IF steel sheet severely deformed by accumulative roll-bonding. Science and Technology of Advanced Materials. 2004;5(1-2):163-72.

22. Jafarian HR, Borhani E, Shibata A, Terada D, Tsuji N. Martensite/austenite interfaces in ultrafine grained Fe–Ni–C alloy. Journal of Materials Science. 2010;46(12):4216-20.

23. Tsuji N, Saito Y, Utsunomiya H, Tanigawa S. Ultra-fine grained bulk steel produced by accumulative roll-bonding (ARB) process. Scripta Materialia. 1999;40(7):795-800.

24. Jafarian H, Borhani E, Shibata A, Tsuji N. Variant selection of martensite transformation from ultrafine-grained austenite in Fe–Ni–C alloy. Journal of Alloys and Compounds. 2013;577:S668-S72.

25. Eizadjou M, Kazemitalachi A, Daneshmanesh H, Shakurshahabi H, Janghorban K. Investigation of structure and mechanical properties of multi-layered Al/Cu composite produced by accumulative roll bonding (ARB) process. Composites Science and Technology. 2008;68(9):2003-9.

26. Mozaffari A, Danesh Manesh H, Janghorban K. Evaluation of mechanical properties and structure of multilayered Al/Ni composites produced by accumulative roll bonding (ARB) process. Journal of Alloys and Compounds. 2010;489(1):103-9.

27. Maier V, Höppel HW, Göken M. Nanomechanical behaviour of Al-Ti layered composites produced by accumulative roll bonding. Journal of Physics: Conference Series. 2010;240:012108.

28. Talebian M, Alizadeh M. Manufacturing Al/steel multilayered composite by accumulative roll bonding and the effects of subsequent annealing on the microstructural and mechanical characteristics. Materials Science and Engineering: A. 2014;590:186-93.

29. Mohammad Nejad Fard N, Mirzadeh H, Mohammad R, Cabrera JM. Accumulative Roll Bonding of Aluminum/Stainless Steel Sheets. Journal of Ultrafine Grained and Nanostructured Materials. 2017;50(1):1-5.

30. Motevalli PD, Eghbali B. Microstructure and mechanical properties of Tri-metal Al/Ti/Mg laminated composite processed by accumulative roll bonding. Materials Science and Engineering: A. 2015;628:135-42.

31. Reihanian M, Naseri M, Jalili Shahmansouri M. Effect of the particle size on the deformation and fracture behavior of Al/4vol.% Al2O3 composite produced by accumulative roll bonding (ARB). Iranian Journal of Materials Forming. 2015; 2(2):14-26.

32. Jamaati R, Naseri M, Toroghinejad MR. Wear behavior of nanostructured Al/Al2O3 composite fabricated via accumulative roll bonding (ARB) process. Materials & Design. 2014;59:540-9.

33. Alizadeh M, Paydar MH. Fabrication of nanostructure Al/SiCP composite by accumulative roll-bonding (ARB) process. Journal of Alloys and Compounds. 2010;492(1-2):231-5.

34. Alizadeh M, Paydar MH, Sharifian Jazi F. Structural evaluation and mechanical properties of nanostructured Al/B4C composite fabricated by ARB process. Composites Part B: Engineering. 2013;44(1):339-43.

35. Salimi A, Borhani E, Emadoddin E. Evaluation of Mechanical Properties and Structure of 1100-Al Reinforced with Zro2 Nano-particles via Accumulatively Roll-bonded. Procedia Materials Science. 2015;11:67-73.

36. Jafarian H, Habibi-Livar J, Razavi SH. Microstructure evolution and mechanical properties in ultrafine grained Al/TiC composite fabricated by accumulative roll bonding. Composites Part B: Engineering. 2015;77:84-92.

37. Ahmadi A, Toroghinejad MR, Najafizadeh A. Evaluation of microstructure and mechanical properties of Al/Al2O3/SiC hybrid composite fabricated by accumulative roll bonding process. Materials & Design. 2014;53:13-9.

38. Farajzadeh Dehkordi H, Toroghinejad MR, Raeissi K. Fabrication of Al/Al2O3/TiC hybrid composite by anodizing and accumulative roll bonding processes and investigation of its microstructure and mechanical properties. Materials Science and Engineering: A. 2013;585:460-7.

39. Naseri M, Hassani A, Tajally M. Fabrication and characterization of hybrid composite strips with homogeneously dispersed ceramic particles by severe plastic deformation. Ceramics International. 2015;41(3):3952-60.

40. Naseri M, Hassani A, Tajally M. An alternative method for manufacturing Al/B4C/SiC hybrid composite strips by cross accumulative roll bonding (CARB) process. Ceramics International. 2015;41(10):13461-9.

41. Fattah-alhosseini A, Naseri M, Alemi MH. Corrosion behavior assessment of finely dispersed and highly uniform Al/B 4 C/SiC hybrid composite fabricated via accumulative roll bonding process. Journal of Manufacturing Processes. 2016;22:120-6.

42. Fattah-Alhosseini A, Naseri M, Alemi MH. Effect of Particles Content on Microstructure, Mechanical Properties,

and Electrochemical Behavior of Aluminum-Based Hybrid Composite Processed by Accumulative Roll Bonding Process. Metallurgical and Materials Transactions A. 2017;48(3):1343-54.

43. Baazamat S, Tajally M, Borhani E. Fabrication and characteristic of Al-based hybrid nanocomposite reinforced with WO 3 and SiC by accumulative roll bonding process. Journal of Alloys and Compounds. 2015;653:39-46.

44. Naseri M, Reihanian M, Borhani E. Bonding behavior during cold roll-cladding of tri-layered Al/brass/Al composite. Journal of Manufacturing Processes. 2016;24:125-37.

45. Hwang Y-M, Hsu H-H, Lee H-J. Analysis of plastic instability during sandwich sheet rolling. International Journal of Machine Tools and Manufacture. 1996;36(1):47-62.

46. Ohsaki S, Kato S, Tsuji N, Ohkubo T, Hono K. Bulk mechanical alloying of Cu–Ag and Cu/Zr two-phase microstructures by accumulative roll-bonding process. Acta Materialia. 2007;55(8):2885-95.

47. Reihanian M, Naseri M. An analytical approach for necking and fracture of hard layer during accumulative roll bonding (ARB) of metallic multilayer. Materials & Design. 2016;89:1213-22.

48. Jamaati R, Toroghinejad MR. Effect of alloy composition, stacking fault energy, second phase particles, initial thickness, and measurement position on deformation texture development of nanostructured FCC materials fabricated via accumulative roll bonding process. Materials Science and Engineering: A. 2014;598:77-97.

49. Kashihara K, Tsujimoto Y, Terada D, Tsuji N. Texture evolution in {112} <111> aluminum single crystals processed by severe plastic deformation. Materials Characterization. 2013;75:129-37.

50. Kamikawa N, Sakai T, Tsuji N. Effect of redundant shear strain on microstructure and texture evolution during accumulative roll-bonding in ultralow carbon IF steel. Acta Materialia. 2007;55(17):5873-88.

51. Kamikawa N, Tsuji N, Minamino Y. Microstructure and texture through thickness of ultralow carbon IF steel sheet severely deformed by accumulative roll-bonding. Science and Technology of Advanced Materials. 2004;5(1-2):163-72.

52. Duan JQ, Quadir MZ, Xu W, Kong C, Ferry M. Texture balancing in a fcc/bcc multilayered composite produced by accumulative roll bonding. Acta Materialia. 2017;123:11-23.

53. Zeng LF, Gao R, Fang QF, Wang XP, Xie ZM, Miao S, et al. High strength and thermal stability of bulk Cu/Ta nanolamellar multilayers fabricated by cross accumulative roll bonding. Acta Materialia. 2016;110:341-51.

54. Carpenter JS, Nizolek T, McCabe RJ, Knezevic M, Zheng SJ, Eftink BP, et al. Bulk texture evolution of nanolamellar Zr–Nb composites processed via accumulative roll bonding. Acta Materialia. 2015;92:97-108.

55. Knezevic M, Nizolek T, Ardeljan M, Beyerlein IJ, Mara NA, Pollock TM. Texture evolution in two-phase Zr/Nb lamellar composites during accumulative roll bonding. International Journal of Plasticity. 2014;57:16-28.

56. Carpenter JS, Vogel SC, LeDonne JE, Hammon DL, Beyerlein IJ, Mara NA. Bulk texture evolution of Cu–Nb nanolamellar composites during accumulative roll bonding. Acta Materialia. 2012;60(4):1576-86.

57. Jamaati R, Toroghinejad MR, Edris H. Effect of stacking fault energy on nanostructure formation under accumulative roll bonding (ARB) process. Materials Science and Engineering: A. 2013;578:191-6.

58. Jamaati R, Toroghinejad MR. Effect of stacking fault energy on deformation texture development of nanostructured

materials produced by the ARB process. Materials Science and Engineering: A. 2014;598:263-76.

59. Jamaati R, Toroghinejad MR. Effect of stacking fault energy on mechanical properties of nanostructured FCC materials processed by the ARB process. Materials Science and Engineering: A. 2014;606:443-50.

60. Wright SI, Nowell MM, de Kloe R, Camus P, Rampton T. Electron imaging with an EBSD detector. Ultramicroscopy. 2015;148:132-45.

61. Kitahara H, Tsuji N, Minamino Y. Martensite transformation from ultrafine grained austenite in Fe–28.5at.% Ni. Materials Science and Engineering: A. 2006;438-440:233-6.

62. Huang X, Tsuji N, Hansen N, Minamino Y. Microstructural evolution during accumulative roll-bonding of commercial purity aluminum. Materials Science and Engineering: A. 2003;340(1-2):265-71.

63. T.H. Courtney, Mechanical Behavior of Materials, Second Ed., McGraw Hill, USA, 2000

64. Borhani E, Jafarian H, Shibata A, Tsuji N. Texture Evolution in Al–0.2 mass%Sc Alloy during ARB Process and Subsequent Annealing. Materials Transactions. 2012;53(11):1863-9.

65. Humphreys FJ, Hatherly M. Recrystallization Textures. Recrystallization and Related Annealing Phenomena: Elsevier; 2004. p. 379-413.

66. Alvand M, Naseri M, Borhani E, Abdollah-Pour H. Microstructure and Crystallographic Texture Characterization of Friction Stir Welded Thin AA2024Aluminum Alloy. Iranian Journal of Materials Science cf. Engineering Vol. 2018;15(1).

67. Quadir MZ, Ferry M, Al-Buhamad O, Munroe PR. Shear banding and recrystallization texture development in a multilayered Al alloy sheet produced by accumulative roll bonding. Acta Materialia. 2009;57(1):29-40.

68. Chang H, Zheng MY, Gan WM, Wu K, Maawad E, Brokmeier HG. Texture evolution of the Mg/Al laminated composite fabricated by the accumulative roll bonding. Scripta Materialia. 2009;61(7):717-20.

69. Hashemipour S, Eivani AR, Jafarian HR, Naseri M, Park N. Microstructure and mechanical properties development of nano/ultrafine grained AISI 316L austenitic stainless steel prepared by repetitive corrugation and straightening by rolling (RCSR). Materials Research Express. 2018;5(12):126519.

70. Gholami D, Imantalab O, Naseri M, Vafaeian S, Fattah-alhosseini A. Assessment of microstructural and electrochemical behavior of severely deformed pure copper through equal channel angular pressing. Journal of Alloys and Compounds. 2017;723:856-65.

71. Naseri M, Gholami D, Imantalab O, Attarzadeh FR, Fattah-Alhosseini A. Effect of grain refinement on mechanical and electrochemical properties of severely deformed pure copper through equal channel angular pressing. Materials Research Express. 2018;5(7):076504.

72. Liu CY, Zhang B, Tang X, Luo K, Ma MZ, Liu RP. Effects of TC4 foil on the microstructures and mechanical properties of accumulatively roll-bonded aluminium-based metal matrix composites. Materials Science and Engineering: A. 2014;615:367-72.

73. Tayyebi M, Eghbali B. Study on the microstructure and mechanical properties of multilayer Cu/Ni composite processed by accumulative roll bonding. Materials Science and Engineering: A. 2013;559:759-64.

74. Meyers MA, Chawla KK. Preface to the Second Edition. Mechanical Behavior of Materials: Cambridge University Press. p. xxi-xxii.